Journal of Photochemistry & Photobiology, A: Chemistry 457 (2024) 115871

Contents lists available at ScienceDirect

Journal of Photochemistry & Photobiology, A: Chemistry

journal homepage: www.elsevier.com/locate/jphotochem

Unravelling the role of silver in addressing the nitrate radical induced photocatalytic oxidation of olefins to epoxides or carbonyl compounds

Alessandro Gottuso [a,*], Filippo Parisi [b,c,*], Davide Lenaz [c], Francesco Parrino [a]

[a] Department of Industrial Engineering, University of Trento, Via Sommarive 9, 38123 Trento, Italy
[b] Babeş-Bolyai University, Faculty of Engineering, Centre for Vibrodiagnostics, Equipment Testing and Automation (CVDTEA), Piaţa Traian Vuia nr. 1-4, 0320003 Reşiţa, Romania
[c] Department of Mathematics, Informatics and Geosciences, University of Trieste, via E. Weiss 8, 34128 Trieste, Italy

ARTICLE INFO

Keywords:
Nitrate radicals
Oxidative cleavage
Epoxidation
Photocatalysis
Silver
TiO_2

ABSTRACT

Nitrate radicals possess the unique capability to add to unsaturated bonds, leading to the formation of carbon-centred radicals evolving to organic compounds, which cannot be achieved through more common reactive oxygen centred species. Therefore, the possibility of generating nitrate radicals through heterogeneous photocatalysis endows this technology with unprecedented possibilities in the field of green organic synthesis. In particular, previous research showcased the promising potential of nitrate radicals in selectively conducting the photocatalytic oxidative cleavage of limonene to limononaldehyde. However, the role of silver ions, required for the reaction to occur, remained uncertain. This study aims at elucidating the role of silver in determining conversion of limonene and selectivity towards the corresponding oxidized compounds. In particular, it has been demonstrated that silver ions efficiently scavenge photogenerated electrons, thus making molecular oxygen available for the nitrate radical induced production of limononaldehyde, obtained with selectivity values up to 60%. In this study it is shown that, nitrate radical formation is as well boosted by silver nanoparticles, in the absence of silver ions. However, in this case, the consequent oxidation of limonene produced both 1,2-limonene epoxide and limononaldehyde. Notably, in the absence of silver ions, molecular oxygen is the main electron scavenger and its lower availability for the oxidative cleavage mechanism addresses the reaction towards the epoxide. *Ab initio* calculations, confirmed this hypothesis, showing that, while formation of limononaldehyde is thermodynamically and kinetically favoured, formation of the epoxide is kinetically limited. Therefore, its formation takes place when the formation of limononaldehyde is hindered by factors such as the reduced availability of molecular oxygen. The identification of key parameters governing the process offers possibilities to tune the selectivity of the reaction towards oxidative cleavage or epoxidation. Moreover, it allows to further optimize this reaction, which may become an appealing and versatile method of chemicals green synthesis.

1. Introduction

The nitrate radical (NO_3) is the most prominent radical compound present in the atmosphere at night-time [1]. While less important than the hydroxyl radical (OH) during the day, due to its relatively low concentration and photo-lability [2], NO_3 is responsible for several oxidative reactions of volatile organic compounds (VOCs) and, in particular, biogenic VOCs (BVOCs), which consist mainly of isoprenoids and monoterpenoids [3]. These reactions represent the most important interactions between anthropogenic and natural emissions since NO_3 is primarily formed at the troposphere level by the direct reaction of nitrogen dioxide (NO_2) with ozone (O_3) [2,4,5]. These chemical transformations can significantly affect air quality, climate, and visibility, resulting in the formation of atmospheric pollutants, such as aldehydes, ketones, organic peroxides, organic nitrates, carbon monoxide, and secondary organic aerosols (SOAs) [6,7]. For these reasons, nitrate radical chemistry has been intensively investigated in the last five decades [5].

Researchers discovered that nitrate radicals can react in the atmosphere via hydrogen atom abstraction transfer (HAT) [8], especially in the case of acidic hydrogen atoms, or selectively via addition to unsaturated carbon–carbon bonds [3,6,8]. The selective addition to these bonds is highly desirable from a technological perspective, since it allows for several synthetic routes, otherwise not achievable with other

* Corresponding authors.
E-mail addresses: alessandro.gottuso@unitn.it (A. Gottuso), filippo.parisi@units.it (F. Parisi).

https://doi.org/10.1016/j.jphotochem.2024.115871
Received 30 March 2024; Received in revised form 18 June 2024; Accepted 28 June 2024
Available online 1 July 2024

common radicals (*i.e.*, hydroxyl radical, alkyl radical, alkoxy radical). Furthermore, the high oxidation potential of nitrate radical (+2.00 V vs. SCE in acetonitrile) [9] could allow for oxidative reactions of a wide range of organic compounds, including alcohols [10], alkenes [11,12], alkynes [13], amines [14], and esters [15], thus increasing the potential applications of NO_3 in fine chemical synthesis. However, practical applications have been discouraged due to the difficult production process of nitrate radicals, as well as their poor stability.

Only recently it has been hypothesized that nitrate radicals could be conveniently produced using the mechanisms underlying heterogeneous photocatalysis. This technology, which has been proven to be a promising tool for sustainable synthesis of fine chemicals at convenient temperature and pressure conditions [16,17], relies on the properties of irradiated semiconductors (*e.g.*, TiO_2) of absorbing light of suitable energy, thus inducing the generation of electron-hole pairs, which eventually promote redox reactions involving electron acceptors and donors in the reacting mixture [18–20].

It has been proposed that nitrate ion (NO_3^-), when in the presence of irradiated TiO_2, can undergo oxidation to nitrate radical through reaction with a photogenerated hole in its free form (h^+) (Eq. (1)), hydrated one (H_2O^+) (Eq. (2)), or trapped on an active site at the photocatalyst surface (Ti-OH^+) (Eq. (3)) [21].

$$NO_3^- + h^+ \rightarrow NO_3 \quad (1)$$

$$NO_3^- + H_2O^+ \rightarrow NO_3 + H_2O \quad (2)$$

$$NO_3^- + Ti - OH^+ \rightarrow NO_3 + Ti - OH \quad (3)$$

In accordance with the existing hypotheses, it has been proposed that photogenerated nitrate radicals can promote the synthesis of molecular bromine (Br_2) from bromine anions (Br^-) in aqueous medium [22] and the efficient production of aldehydes from primary alcohols in acetonitrile [23,24], through the HAT mechanism. In our previous works [25–27], we suggested that nitrate radicals photocatalytically generated promote oxidative cleavage of various olefins to the corresponding carbonyl compounds, according to an addition mechanism to unsaturated carbons.

In particular, the addition of a nitrate radical to the double bond leads to a carbon-centred radical which in turn undergoes subsequent addition of molecular oxygen, forming a peroxyalkyl radical ($ROO^\bullet$). The latter, upon further reaction with a nitrate radical (or another peroxyalkyl radical), evolves into an alkoxide radical ($RO^\bullet$), which can undergo oxidative cleavage of the original carbon–carbon double bond, forming two carbonyl groups [25–27]. It is important to highlight here, for the aims of the present work, that the presence of molecular oxygen is essential for this reaction to occur, along with the simultaneous presence of silver and nitrate ions.

However, despite these significant advancements, the precise mechanisms by which these ions operate remained shrouded in ambiguity. Furthermore, the environmentally and economically unfavourable use of sacrificial silver poses substantial challenges for industrial-scale implementation and future applications. Consequently, it is imperative to shine light on the intricate mechanistic insights of this reaction, in order to propose more sustainable alternatives to silver ions. For these reasons, the aim of this study is to unravel the multifaceted role of silver in its ionic and metallic form in determining the process selectivity and conversion, in correlation with the other reaction components, including molecular oxygen and nitrate radicals. In this scenario, *ab initio* calculations have been performed to provide thermodynamic and kinetic information to complement and corroborate the experimental results. By identifying the salient factors and evaluating potential alternatives, we aim at enhancing the industrial allure and feasibility of harnessing nitrate radicals for the synthesis of fine chemicals, potentially paving the way towards a more sustainable and industrially appealing approach.

2. Experimental part

2.1. Materials

Titanium dioxide (TiO_2, anatase 73–85 %, rutile 14–17 %, amorphous 0–13 %, P25 Evonik), lithium nitrate ($LiNO_3$, 99.0 %, Sigma-Aldrich), silver nitrate ($AgNO_3$, 99.8 %, Carlo Erba), *R*-limonene (d = 0.844 g/mL, 97 %, Sigma-Aldrich), gold chloride ($AuCl_3$, 99.9 % Sigma-Aldrich), palladium chloride ($PdCl_2$, 99.9 % Sigma-Aldrich), hexachloroplatinic acid ($H_2PtCl_6{\cdot}xH_2O$, 99.9 %, Pt 37–40 %, Sigma-Aldrich), rhodium chloride ($RhCl_3$, 98 % Sigma-Aldrich), methanol (d = 0.792 g/mL, 99.9 %, PanReac-AppliChem ITW Reagents) acetonitrile (d = 0.78 g/mL, anhydrous, 99.8 %, Sigma-Aldrich), ethanol (d = 0.789 g/mL 99.8 %, Fluka), deionized water (<1.5 μS/m) were used without further purification.

2.2. Photodeposition of noble metal nanoparticles onto TiO_2

Noble metal-decorated TiO_2 samples, labelled as M−TiO_2 (M=Au, Ag, Pd, Pt, Rh) were prepared by a one-step UV light induced deposition method. The noble metal precursor (ca. 10 wt%) was added to 50 mL of a methanolic (20 % v/v in H_2O) suspension containing 100 mg of TiO_2. The mixture was sonicated for 15 min, degassed with N_2 in dark under vigorous stirring for 90 min, and irradiated by means of 6 actinic lamps (Philips, 15 W each, λ_{max} = 365 nm, total radiant flux 40.15 W/m^2) placed hexagonally around the batch reactor for 120 min. The suspension was then centrifuged (4500 rpm, 15 min) to recover the product, which was rinsed three times with a mixture of ethanol/water 1:1 and then three times with only water. Finally, the powder was dried in a vacuum oven at 80 °C overnight. Samples were characterized by Transmission Electron Microscopy (TEM), and X-ray Diffraction (XRD).

2.3. Photocatalytic tests

In a representative run under UV light irradiation, 0.5 g/L of photocatalyst were dispersed in an acetonitrile solution containing *R*-limonene 2 mM. In the presence of bare TiO_2 as the catalyst, $AgNO_3$ (10 mM) or variable amounts of Ag_2SO_4 and $LiNO_3$ (10 mM) were dissolved in the reaction medium. In the presence of Ag-TiO_2 sample (0.5 g/L), only $LiNO_3$ (10 mM) was added. The mixture was sonicated for 15 min at room temperature. The obtained suspension was then irradiated, under vigorous stirring, by UV-A light in a Pyrex batch reactor equipped with six actinic lamps (Philips, 15 W each, λ_{max} = 365 nm, total radiant flux 40.15 W/m^2). Runs under visible light irradiation were performed in a cylindrical reactor (with a diameter of 4 cm) containing 150 ml of the suspension irradiated by means of a tungsten-halogen lamp (Wolfram, 60 W) placed axially and immersed in the photocatalytic suspension. The lamp was surrounded by a thimble in which a thermostated (25 °C) 1 M $NaNO_2$ aqueous solution was recirculated, in order to keep constant the reaction temperature and to cut-off the radiation at wavelengths lower than 400 nm. Samples of the reaction mixture were withdrawn at fixed times, filtered (PTFE syringe filter, 0.2 μm), and analyzed by means of a GC-2010 Pro (Shimadzu, Kyoto, Japan) equipped with an AOC-20i auto-injector and FID detector and by using a HP5-MS, 5 % diphenyl-95 % dimethylpolysiloxane capillary column (30 m, 0.25 mm, 0.25 μm film thickness). Chromatographic conditions: 1 μL split 1:25 injection by autosampler, carrier gas N_2 at 3.0 mL/min, injector temperature 250 °C. Oven temperature program: 1 min of 40 °C isotherm followed by a linear temperature increase of 12 °C/min up to 200 °C held for 5 min, followed by an increase of 15 °C/min up to 280 °C. Standard mixtures of selected identified standard compounds were also injected to obtain quantitative responses. n-Octane was used as internal standard for quantitative analyses.

2.4. Characterization techniques

TEM images were recorded on a Philips EM 208 microscope operating at 100 kV and equipped with an 11 MP bottom-mounted CCD Olympus Quemesa camera. Samples were ground in an agate mortar and suspended in ethanol. The solutions were transferred onto TEM carbon grids and dried in vacuum. S/TEM micrographs were acquired by using a scanning electron microscope Zeiss Gemini300, equipped with the EDS probe Burker XFlash 610 M at the working distance of 4.3 mm using an acceleration voltage of 20 kV.

Powder XRD patterns were obtained by using a diffractometer in Bragg–Brentano geometry equipped with a Cu anode source (Kα, λ = 1.54056 Å, voltage 40 kV, current 30 mA) coupled to a multilayer collimating monochromator (Goebel mirror). Samples were positioned in reflection geometry with a fixed angle of 10° angle with respect to the incident beam and the diffraction patterns were acquired by means of a Dectris Mythen 1 K hybrid pixel detector with typical 10–100° 2θ range, steps of 0.05° and acquisition time of 5 s/step. The instrument resolution (divergent and antiscatter slits of 0.5°) was determined using standards free from the effect of reduced crystallite size and lattice defects.

2.5. Computational methodologies

Density functional theory (DFT) was used for geometry optimizations of all minima and transition states at the Becke's three-parameter hybrid method employing the Lee-Yang-Parr correlation function (B3LYP) [28,29]. The B3LYP geometries were optimized using the 6-31+G(d,p) basis set and characterized by harmonic frequency analyses at the same theory level. Minima were identified by having no imaginary frequencies, while transition states, optimized by means of Berny algorithm, were identified by having one, and only one, imaginary frequency along the relative reaction coordinate. For all the geometries, different spin multiplicities have been taken into account and the more energetically stable ones have been considered for further computations. Single-point-energy (SPE) calculations of the optimized geometries were performed using second-order Møller-Plesset perturbation theory (MP2) [30] and coupled-cluster level theory with full treatment on single and double excitations, while triple excitation contributions were implemented with perturbation-theory arguments (CCSD(T)) [31]. Basis sets belonging to the 'correlation-consistent' family of Dunning and co-workers [32] were implemented for SPE calculations; specifically, cc-pVDZ was used for CCSD(T) theory level calculations, while cc-pVDZ, aug-cc-pVDZ and aug-cc-pVTZ for MP2 ones. The single point energies calculated at the CCSD(T)/cc-pVDZ level were then extended to the complete basis set (CBS) through an MP2 extrapolation formula reported in Eq. (4).

$$E_{CCSD(T)/CBS} = E_{CCSD(T)/cc-pVDZ} + E_{MP2/aug-cc-pVTZ} - E_{MP2/cc-pVDZ} + 0.463(E_{MP2/aug-cc-pVTZ} - E_{MP2/aug-cc-pVDZ}) \quad (4)$$

This extrapolation scheme has been proven to be accurate and comparable to other more computationally expensive cc-pVDZ/cc-pVTZ extrapolation schemes [33,34]. For all computations, solvent was implemented using the solvation model based on density (SMD) described by Truhlar and co-workers [35]. Corrections for the zero-point energy (ZPE) at B3LYP/6-31+G(d,p) level was implemented to all energies. For all the calculations performed, unrestricted formalism was employed. In this regard, it is worth mentioning that unrestricted formalism along with coupled-cluster method, which is known to give spin contamination issues for similar systems, has been proven to be suited for similar monoradical systems [34,36,37]. All the computations were performed by using the Gaussian 16 suite of programs [38].

3. Results and discussion

Conversion of *R*-limonene and selectivity towards *R*-limononaldehyde (LA) obtained under UV irradiation of suspensions containing bare TiO_2, a constant amount of $LiNO_3$ (10 mM) and variable amounts of Ag_2SO_4 ranging from 0 to 5 mM, are reported in Fig. 1.

Results in Fig. 1 show that the presence of silver ions in the suspension reduces the conversion of limonene. However, increasing the amount of Ag_2SO_4 from 1.25 to 5 mM results in slight increasing conversion values. On the other hand, while only traces of LA (<3% selectivity) have been detected in the absence of silver ions, selectivity towards LA increases by increasing their amount, reaching a value of approximately 50 % for the highest concentration of Ag^+ used. The selectivity trend remains consistent across all cases, exhibiting a maximum peak at around 60 min, followed by a decline for prolonged irradiation times. This characteristic behaviour, commonly observed in partial oxidation reactions [39–41], is ascribed to the prevailing over-oxidation of products surpassing the rate of their generation. As elucidated in our previous report [25], LA is the main product, while the residual conversion entails the barely detectable formation of other partial oxidized products and the complete oxidation of the organic substrates, ultimately yielding carbon dioxide. The formation of LA, resulting from the oxidative cleavage of endocyclic carbon–carbon double bond of limonene, is linked to the formation of nitrate radical, generated through hole-induced mechanisms. LA formation occurs significantly only in the simultaneous presence of silver and nitrate ions; therefore, it has been speculated that the nitrate radical formation occurs more efficiently in the presence of silver ions. However, further clarification regarding the exact function of the latter is required, as described below.

Results in Fig. 1, highlight the role of silver ions in improving the selectivity of the oxidative cleavage to LA, being constant the amount of nitrate ions present in the solution. It has to be noted that, along with silver ion, also the concentration of the sulphate counterion increases, and competitive interactions between the NO_3^- and SO_4^{2-} ions with the

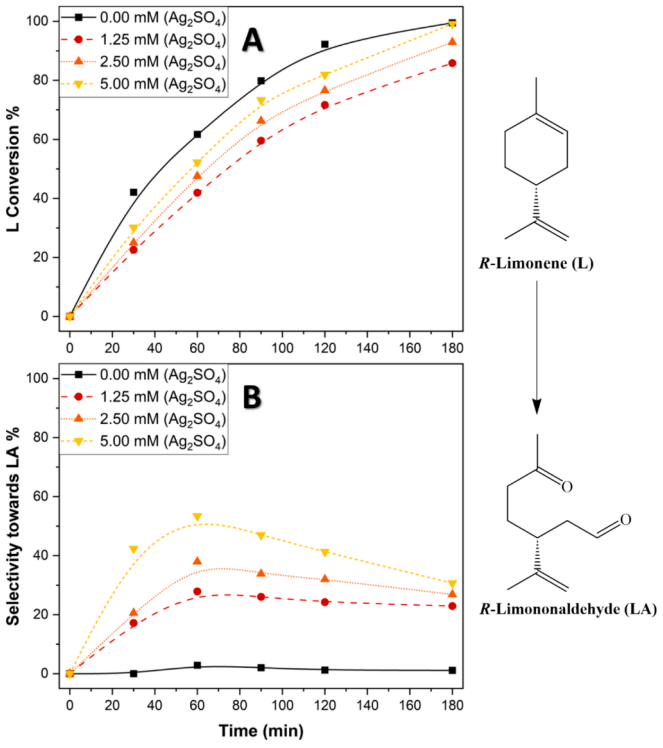

Fig. 1. *R*-Limonene (L) conversion (Panel A) and selectivity towards *R*-limononaldehyde (LA) (Panel B) at constant amount of bare TiO_2 (0.5 g/L) and $LiNO_3$ (10 mM), by variating the concentration of Ag_2SO_4, *i.e.* 0 mM (black squares), 1.25 mM (red circles), 2.5 mM (orange upward triangles), 5.0 mM (yellow downward triangles).

catalyst surface cannot be excluded. However, the effect of sulphate ions is not dramatically limiting the reaction performance, as the selectivity towards LA in the absence of sulphate ions, keeping constant all of the other experimental conditions, reaches a maximum of ca. 60 %, which is comparable with the result hereby reported. Moreover, the presence of sulphate did not alter the product distribution, being its hole-scavenging capability lower compared with nitrate ions [21]. A comparison of the run with and without sulphate ions is shown in the Supporting Information (Fig. S1).

The notable conversion observed in the absence of silver ions suggests that limonene tends to react with the photogenerated holes, resulting in its non-selective oxidation, in agreement with the negligible production of LA. Conversely, it has been demonstrated that the fate of silver ions in this system is their photoreduction at the surface of excited TiO_2 [25], leading to the formation of nanometric metallic silver particles on the surface.

To further confirm the continuous deposition of silver nanoparticles (Ag^0) during the reaction, the catalyst was separated from the reaction medium after two separated runs lasting 60 and 120 min, respectively, dried at 80 °C in oven and finally analysed by transmission electron microscopy (TEM). Fig. 2, shows the obtained TEM images, along with the one of bare TiO_2, for the sake of comparison.

Fig. 2 clearly shows that the amount of metallic silver nanoparticles at the surface of TiO_2 increases with the irradiation time. Accordingly, the suspension turns from white to light brown after few minutes and becomes slowly and increasingly darker. The size reduction of silver nanoparticles observed at longer irradiation times (Panel C) can be ascribed to a parasitic reaction of silver nanoparticles with CN radicals arising from acetonitrile photodegradation. Nonetheless, as demonstrated in a previous work by means of Rietveld refinement of the acquired powder XRD patterns [25], this reaction can be safely neglected during the first two hours of irradiation, as it becomes macroscopically relevant only after the complete conversion of limonene (after 120 min).

The continuous deposition of silver nanoparticles above demonstrated, however, has still to be convincingly bound to the observed selectivity trends towards LA (Fig. 1). Some hypotheses in this regard will be hereby discussed.

Silver, in its metallic or ionic form, may play different roles in the present reaction, eventually influencing the final product distribution:

i) catalytic localized surface plasmon resonance (LSPR) or thermal catalytic effects induced by silver nanoparticles;
ii) electron-sink effect of silver nanoparticles;
iii) electron-acceptor effect of silver ions.

In order to ascertain the effect of silver nanoparticles and to separate their contribution from the effect of silver ions reduction, we performed the reaction in the presence of a TiO_2 sample, labelled as Ag-TiO_2, predecorated with silver nanoparticles, according to a method elsewhere reported [42] and described in the experimental section. Notably, the prior photo-deposition of silver is crucial, since it cannot be achieved without UV light irradiation. The Ag-TiO_2 sample has been characterized by means of S/TEM and XRD analysis and results are reported in Figs. 3 and 4, along with the ones related to the photocatalyst recovered after 60 min of irradiation in a representative run carried out in the presence of $AgNO_3$ (10 mM).

Given the aleatory nature of particle growth process, lognormal distribution has been considered for the fitting of the reported histograms. The prior photodeposition of silver allowed for a narrower diameter distribution of silver nanoparticles ($\sigma = 0.30$) if compared to the one formed during the reaction after 60 min of irradiation ($\sigma = 0.39$). Samples show similar XRD pattern, constituted by the typical signals of TiO_2 (P25) anatase and rutile phases and of those related to metal silver nanoparticles, as indicated in Fig. 4. The broader distribution of silver nanoparticles is deducible also in the diffraction patterns, where a greater intensity of metallic silver diffraction peaks, even if in slight, can be observed. Nonetheless, both samples display almost the same mean diameter ($\mu_A = 51$ nm; $\mu_B = 56$ nm) as shown in Fig. 3. Therefore, the two materials can be considered comparable and used to check the mechanistic hypotheses mentioned above.

In the first scenario, silver nanoparticles could act as thermal catalysts for the reaction [43]. On the other hand, they could lead to LSPR phenomena, as widely reported in literature [44,45], due to the visible light absorption within the range of 450 to 550 nm [25]. In fact, LSPR results in the collective oscillation of conduction electrons in response to the electric field of the adsorbed light, eventually generating a localized electromagnetic field at the surface of the nanoparticles, eventually leading to charge separation. The LSPR effect is highly dependent on the size, shape, and material composition of the nanoparticles [46]. Even if the underlying mechanisms are still under debate [47–49] and may involve hot electron transfer, local field enhancement or energy transfer from the plasmonic nanostructure to the semiconductor, there are evidences that this effect may trigger competitive or cooperative oxidation mechanisms in conjunction with those induced by photo-irradiated TiO_2 [44]. In order to check the existence of thermal or LSPR induced catalytic effects on the selectivity of the present reaction, runs have been carried out in the presence of Ag-TiO_2 and $LiNO_3$ (10 mM) as described in the experimental part, under dark conditions or under visible light irradiation. Limonene remained nearly stable both under dark (nearly no conversion) and visible light (conversion < 8 % after 180 min of reaction). These results indicate that the photocatalytic process is exclusively promoted by excited TiO_2. Therefore, the role of the metal nanoparticles as thermal or plasmonic catalysts can be excluded, or at least assumed to be not relevant.

Therefore, silver may assume two primary functions: electron acceptor in the form of silver ions and electron-sink in the form of silver nanoparticles. Attempts to substitute silver ions with other electron acceptors (such as $NaBrO_3$, SF_6, or $KHSO_5$) failed, due to unavoidable side reactions involving these compounds. Therefore, in order to independently evaluate these effects, even if indirectly, we compared the performances in terms of conversion of limonene and selectivity towards LA of the reaction in the presence of (i) bare TiO_2 and 10 mM $AgNO_3$ (dotted lines in Fig. 5), and (ii) Ag-TiO_2 and 10 mM $LiNO_3$ (solid lines in Fig. 5). The electron-sink effect of silver nanoparticles was also compared with other noble metals, using different pre-decorated TiO_2 samples (M−TiO_2; M=Au, Pd, Pt, Rh) obtained with the same predeposition method and used for representative runs. Results are reported in Fig. S4. The limonene conversion and selectivity towards the oxidized compounds did not change significantly in the presence of the different noble metal nanoparticles. This result indicates that, notwithstanding the different work functions of the tested noble metals, the electron sinking step is possibly too fast in all of the cases to be the rate determining one for this reaction.

As shown in Fig. 5, the reaction carried out with the Ag-TiO_2 catalyst reaches a conversion rate of approximately 90 % after 10 h of UV-A light irradiation, while the reaction in the presence of $AgNO_3$ is much faster (>99 % conversion after 180 min). Interestingly, unlike the case with $AgNO_3$, where a maximum value of ca. 60 % selectivity towards LA was reached after ca. 60 min, the selectivity towards LA is significantly reduced, reaching a maximum of around 16 % after 6 h. Remarkably, the prior silver deposition yielded an unexpected outcome, resulting in the production of 1,2-limonene epoxide (1,2-LO; endo/exo ratio ca. 2.2, see Fig. S2) with higher selectivity than *R*-limononaldehyde, reaching a maximum of approximately 27 % within 6 h of irradiation, while in the reaction performed starting with Ag^+ the epoxide species could be barely detected.

Some general consideration on the results of the two runs, in the presence of silver ions (dotted lines) and in the presence of pre-deposited metallic silver (solid lines) is required before discussing the results in detail. Even if in both cases recombination is reduced and hole-induced phenomena, such as nitrate radical formation, are promoted, very different scenarios can be envisaged with respect to the electron

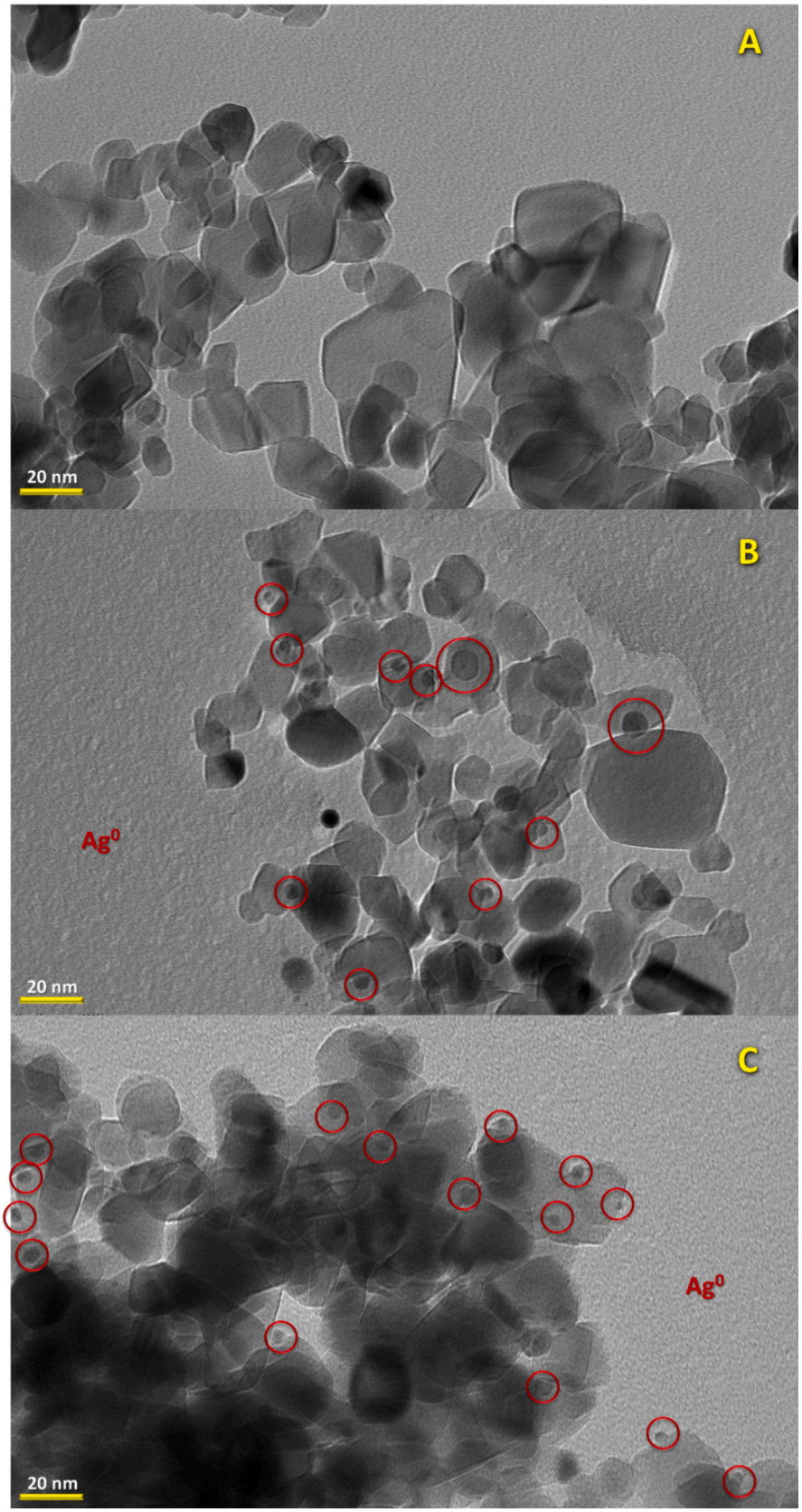

Fig. 2. (Panel A) TEM micrograph of the pristine TiO_2 catalyst; (Panel B) Catalyst recovered after 60 min of irradiation in the presence of $AgNO_3$ 10 mM and *R*-limonene 2 mM in acetonitrile; (Panel C) Catalyst recovered after 120 min of irradiation in the presence of $AgNO_3$ 10 mM and *R*-limonene 2 mM in acetonitrile.

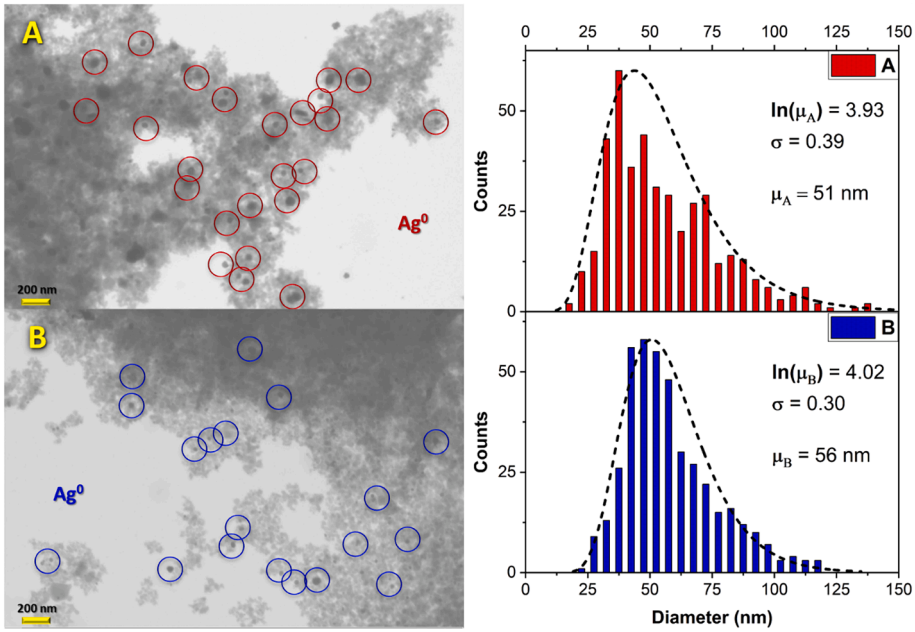

Fig. 3. (Panel A, left) S/TEM micrograph of the TiO_2 catalyst recovered in a representative run after 60 min of irradiation, in the presence of $AgNO_3$ 10 mM, and *R*-limonene 2 mM in acetonitrile; (Panel B, left) S/TEM micrograph of the Ag-TiO_2 sample. (Right Panel) Histograms of silver nanoparticles diameter and lognormal distribution of both the catalysts reported in Panel A (red) and Panel B (blue).

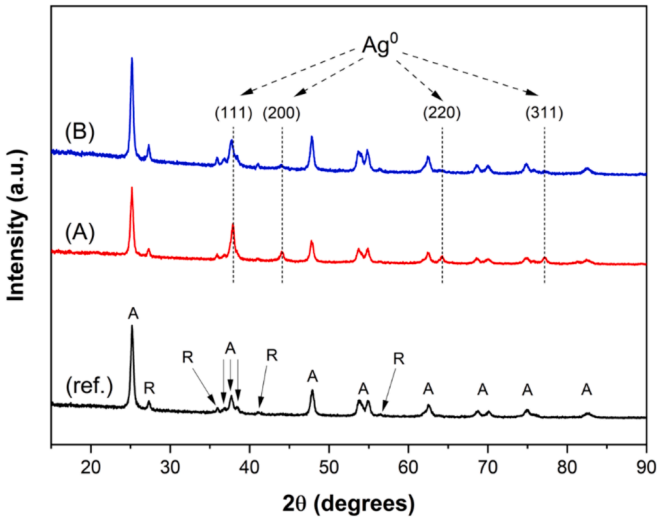

Fig. 4. Powder XRD patterns of ref.) pristine TiO_2, A) TiO_2 after 60 min of irradiation in a representative run, and B) Ag-TiO_2 sample.

availability in the system. In fact, in the first case silver ions scavenge photogenerated electrons much more efficiently than oxygen due to the more favourable thermodynamic features (E^0 $Ag^+_{(aq)}/Ag^0 = 0.799$ V vs SHE; E^0 $O_{2(aq)}/O_2^-{}_{(aq)} = -1.00$ V vs SHE) [50,51]. This results in a system where oxygen in its molecular form is more available and can intervene in the reaction mechanism for the production of LA, as described in the introduction section. On the other hand, in the second case electrons are only conveyed to the silver nanoparticles, from which they can easily reduce oxygen as the electron scavenger. Therefore, in this case, the reduced availability of molecular oxygen should limit the production of LA.

These considerations are confirmed by the results in Fig. 5. In fact, the presence of pre-deposited metallic silver on the catalyst, in the absence of silver ions, greatly reduces both the conversion and the path of the oxidative cleavage of C=C bonds towards LA. The reduced conversion can be tentatively attributed to the lower electron scavenging capability of oxygen with respect to silver ions, as above mentioned. The lower selectivity towards LA possibly derives from the reduced availability of molecular oxygen, which is essential for the generation of LA. Consequently, it can be inferred that the sacrificial reduction of silver ions is crucial for the selectivity of the process towards LA.

On the other hand, limonene epoxidation takes place significantly in the presence of pre-deposited silver, while it is negligible in the presence of silver ions. Existing literature highlights that the formation of epoxides from alkenes could be achieved under photocatalytic conditions through the generation of singlet oxygen ($^1O_2$), which eventually adds to the double bonds, leading to epoxide formation via [2 + 2] cycloaddition mechanisms or Schenck-ene reaction [52–55]. In fact, previous studies have shown that, in heterogeneous photocatalysis, the efficient generation of singlet oxygen is likely triggered by energy transfer processes prevailing over interfacial electron transfer [56–58]. However, it has been also hypothesized that nitrate radicals may promote the generation of epoxides. Wayne *et al.*, for example, suggested that upon the introduction of nitrate radicals, the resultant adduct could undergo concerted rearrangement to form an epoxy ring. This process would be accompanied by homolytic cleavage of the O-NO_2 bond, leading to NO_2 elimination as per Eq. 5.

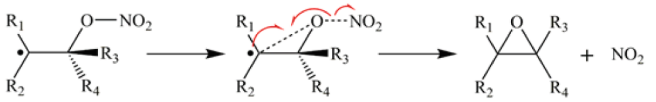

(5)

To test this hypothesis and elucidate the potential influence of nitrate radicals on epoxide formation, additional experiments were conducted to isolate the contributions of the individual components. Specifically, these tests were carried out in the absence of nitrate radicals or under a nitrogen flow. Fig. 6 presents a comparative assessment of limonene conversion and epoxide selectivity under diverse reaction conditions.

In the presence of the silver pre-decorated catalyst (Ag-TiO_2) but in the absence of nitrates, limonene conversion proceeded rapidly, reaching completion within 5-hour irradiation and providing a maximum LO selectivity of approximately 17 %. This suggests that LO can indeed

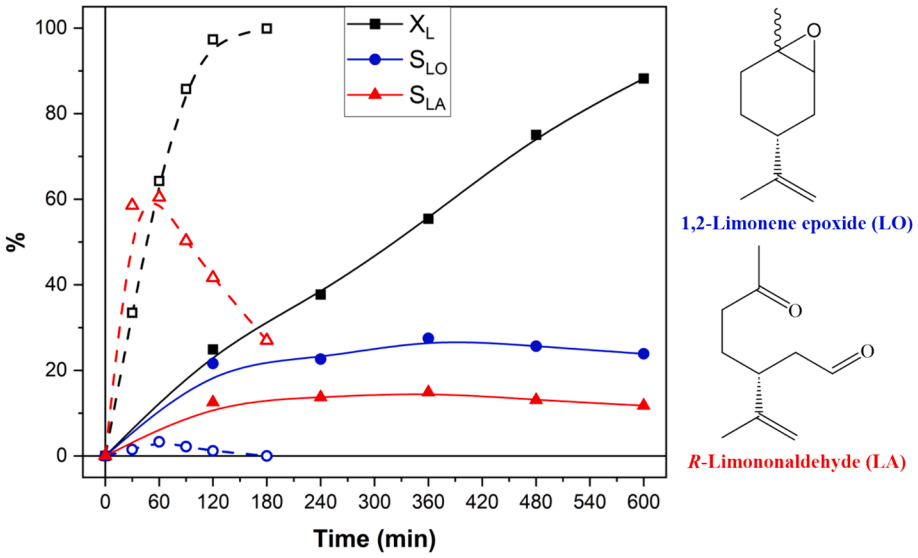

Fig. 5. *R*-Limonene conversion (X_L; black squares), selectivity towards 1,2-limonene epoxide (LO) (S_{LO}; blue circles), selectivity towards *R*-limononaldehyde (LA) (S_{LA}; red triangles). Reaction conditions for solid line trends: *R*-limonene 2 mM, $LiNO_3$ 10 mM, Ag-TiO_2 0.5 g/L in acetonitrile. Reaction conditions for dashed line trends: *R*-limonene 2 mM, $AgNO_3$ 10 mM, bare TiO_2 0.5 g/L in acetonitrile.

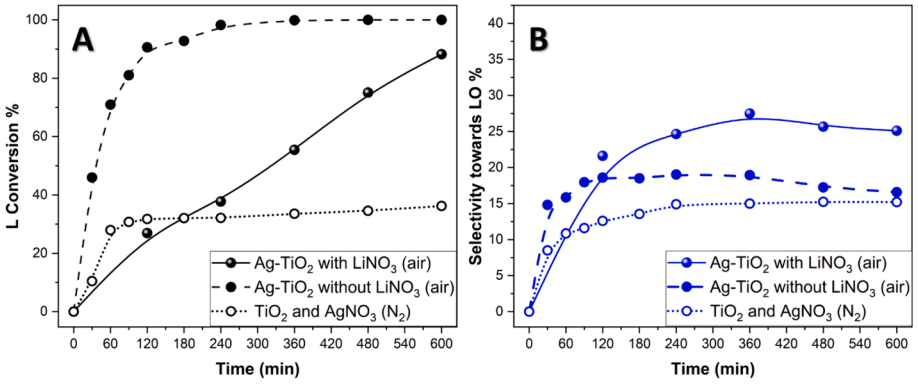

Fig. 6. Conversion of *R*-limonene (L) (Panel A, black curves) and selectivity towards 1,2-limonene epoxide (LO) (Panel B, blue curves) under different reaction conditions: Solid line trends: *R*-limonene 2 mM, $LiNO_3$ 10 mM, Ag-TiO_2 0.5 g/L under static air in acetonitrile. Dashed line trends: *R*-limonene 2 mM, Ag-TiO_2 0.5 g/L under static air in acetonitrile. Dotted line trends: *R*-limonene 2 mM, $AgNO_3$ 10 mM, TiO_2 0.5 g/L under N_2 in acetonitrile.

originate from the reaction involving molecular oxygen. Accordingly, Hu *et al.* [59] report that decoration of TiO_2 with metal nanoparticles promotes the formation of singlet oxygen. This behaviour sharply contrasts with the results obtained in the analogous experiment involving nitrates, both in terms of conversion kinetics and selectivity. In fact, the presence of nitrates inhibits the direct oxidation of limonene by photogenerated holes, instead promoting controlled oxidation. Therefore, a concomitant role of nitrate radicals cannot be excluded. To reveal the existence of a nitrate radical induced epoxidation mechanism, a reaction was performed with TiO_2 and $AgNO_3$ in the virtual absence of oxygen, by bubbling nitrogen throughout the suspension. It is crucial to underline that the presence of silver ions is essential, as they act as scavengers for photogenerated electrons. Under these conditions, the reaction yielded rapid but limited limonene conversion, with 15 % selectivity towards the epoxide. Notably, no limononaldehyde formation could be observed in these conditions, being the presence of oxygen required for the oxidative cleavage. The detection of limonene epoxide in the absence of oxygen suggests that nitrate radicals can indeed trigger epoxidation, thus corroborating the hypothesis of Wayne *et al.*

In conclusion, experimental results suggest that 1,2-limonene epoxide (LO) formation could take place concurrently with or in parallel to the oxidative cleavage reaction of the double bond, being both reactions induced by nitrate radicals.

Addressing the reaction towards the carbonyl or epoxide compounds, therefore, depends on the different availability of molecular oxygen and to possible kinetic limitations. In order to validate the hypothesis on the role of molecular oxygen, a test in the presence of Ag-TiO_2 and $LiNO_3$, was carried out by bubbling a gaseous stream of pure molecular oxygen at a pressure of 1 atm, instead of air. Results, shown in the Supporting Information (Fig. S3), demonstrate that a greater amount of available oxygen in the reaction mixture leads to higher limonene conversion, while addressing selectivity towards LA (LO/LA ratio decreases from 1.7 to 1.4). This observation indicates a dual role of molecular oxygen: when present in larger amounts, it promotes as an electron scavenger the conversion of limonene and as a reactant the generation of LA. These findings offer additional validation for the proposed mechanisms.

Notably, the significant formation of the epoxide exclusively observed in tests conducted with Ag-TiO_2, along with the remarkable suppression of LA production, indicates that the nitrate radical induced ring closure path to the epoxide is kinetically disadvantaged compared to the oxidative cleavage. In order to verify this hypothesis and to complement the experimental findings, computational calculations were conducted to unravel the thermodynamic and kinetic aspects of the

proposed mechanisms of formation of *R*-limononaldehyde and 1,2-limonene epoxide, both induced by nitrate radicals.

It is important to emphasize that this study focuses only on the competition between the two mechanisms leading to the formation of epoxide or limononaldehyde. Therefore, the calculated stationary and transition states are primarily those contributing to the chemical species and intermediates that lead to the experimentally observed products. For these reasons, the addition of the nitrate radical to the endocyclic double bond of limonene was examined by considering all of its possible geometries as depicted in Fig. 7, while the addition of the nitrate radical to the exocyclic double bond of limonene will not be considered. In fact, in agreement with our results, previous computational and experimental investigations have suggested that the addition of nitrate radical on the exocyclic double bond of *R*-limonene is both thermodynamically and kinetically unfavoured with respect to the one on the endocyclic double bond [36,60].

Table 1 presents the energy values of the four stationary intermediate states (INT) depicted in Fig. 7 and the corresponding transition states (TS), obtained as the difference with the computed energy of *R*-limonene-NO_3 separated system, through calculations at various theoretical levels with zero-point energy (ZPE) corrections. Specifically, the UB3LYP/6-31+G(d,p) level was used for the ZPE correction. Fig. 8 illustrates the potential energy surface (PES) concerning the addition of the nitrate radical to the carbons involved in the endocyclic double bond. The PES was calculated using the CCSD(T)/CBS level of theory with ZPE correction at the UB3LYP/6-31+G(d,p) level.

For each carbon, we examined additions with endo- and *exo*-geometry, considering the chirality of the starting compound (*R*-limonene). The UB3LYP/6-31+G(d,p) level was used to investigate several bond angles, and only the thermodynamically most stable configurations for each geometry were selected for more accurate calculations. It is noteworthy that the NO_3 specie was modelled and optimized at the UB3LYP/6-31+G(d,p) level, assuming a radical in a doublet state with D_{3h} geometry. An interatomic N-O distance of 1.23 Å was calculated, in agreement with the relevant literature [5]. Furthermore, it should be emphasized that, when performing calculations at the MP2 level, we considered the energies calculated with the projection of spin eigenvalues (PMP2) [61,62]. This choice was made due to the presence of non-negligible spin contamination for the unrestricted wavefunctions at the MP2 level (Table S1).

The adducts resulting from the addition of NO_3 to limonene in all investigated geometries exhibit significantly lower energy than the separate reactants (*R*-limonene + NO_3), with values ranging from −16.24 to −18.73 kcal/mol. These results suggest that the nucleophilic addition of the nitrate radical is energetically favourable for all of the four proposed geometries with no significant differences, being just a discrepancy of around 2 kcal/mol. Additionally, an elongation of the C_1-C_2 bond is observed (from 1.33 Å in *R*-limonene to values ranging from 1.47 to 1.50 Å in the intermediate states) upon the approach and addition of the nitrate radical to the carbon–carbon double bond. This elongation implies partial loss of the double bond character. We also observed elongation of the O-NO_2 bond (from 1.23 Å in NO_3 to values between 1.38 and 1.41 Å), resulting in a reduction of the ON-O_2 bonds (interatomic distances from 1.23 Å in NO_3 to 1.21 Å) not involved in the formation of the C-O bond, leading to the loss of D_{3h} symmetry.

Negative values have been observed for all of the four transition states. The latter are expected to exhibit higher energy values than both reactants and products. The calculated negative values, with respect to non-interacting reactants, suggest the presence of local minima at lower energy levels, corresponding to weakly-bonded Van der Waals complexes [63–65]. These complexes likely form barrier-less interactions of the nitrate radical with the π electrons of the double bond, consistently with findings in similar A + B → C reactions [66–68]. It is crucial to note that activation barriers should be calculated in relation to the energy of these pre-reaction complexes. However, computational studies on comparable systems, employing more precise levels of theory for

Table 1
R-Limonene-NO_3 reaction energies with ZPE correction (kcal/mol) included computed at different levels of theory for the four different additions to endocyclic C=C double bond[a]. All the values have been obtained as the difference with the computed energy of *R*-limonene-NO_3 separated system.

Geometries	UB3LYP/6-31+G(d,p)	PMP2/cc-pVDZ	PMP2/aug-cc-pVDZ	PMP2/aug-cc-pVTZ	CCSD(T)/cc-pVDZ
TS-C_1 endo	−6.06	12.84	7.62	9.70	−3.94
TS-C_1 exo	−5.21	8.81	4.13	6.34	−5.81
TS-C_2 endo	−6.68	11.95	6.80	8.68	−3.47
TS-C_2 exo	−8.61	11.82	6.54	8.22	−4.76
INT-C_1 endo	−10.69	−9.43	−12.74	−11.13	−18.49
INT-C_1 exo	−8.53	−6.87	−9.94	−8.45	−17.12
INT-C_2 endo	−11.83	−10.96	−13.11	−11.44	−20.09
INT-C_2 exo	−11.55	−9.52	−12.24	−10.54	−18.92

[a] Geometry optimization and frequency analysis at the UB3LYP/6-31+G(d,p) level.

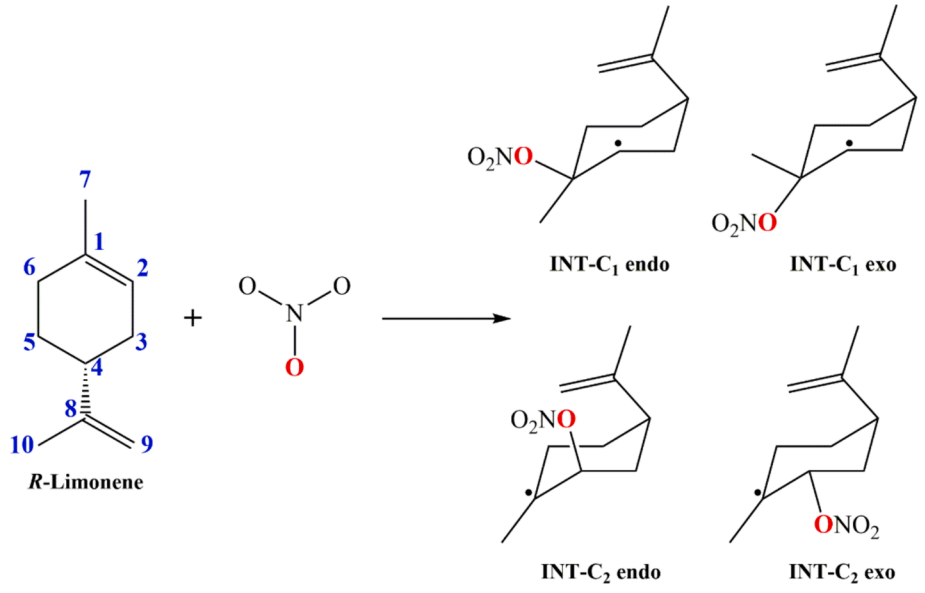

Fig. 7. Schematic representation of the possible additions of the nitrate radical to the endocyclic double bond of *R*-Limonene.

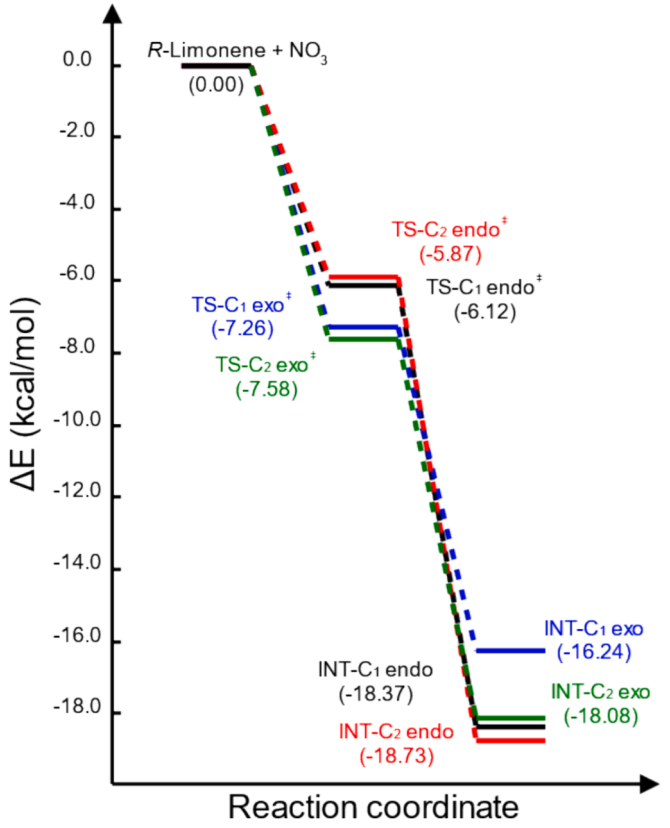

Fig. 8. PES at CCSD(T)/CBS level with ZPE correction at UB3LYP/6-31+G(d,p) level of NO_3 addition to endocyclic C=C double bond of *R*-limonene.

geometry determination of long-range interacting complexes (e.g., M06-2X/aug-cc-pVTZ, M06-2X/6-311++G**), have yielded energy values which differ from the relative transition state energies of approximately 1–2 kcal/mol. These findings suggest all four geometries are nearly equivalent at room temperature from a kinetic standpoint, which observation is in agreement with the experimental presence of both exo- and endo- isomers of 1,2-limonene epoxide in the products yield. Further analysis at the CCSD(T)/CBS level revealed that the nitrate radical predominantly adds to the less substituted carbon. Thus, starting from the most thermodynamically stable adduct (INT-C_2 endo), we explored reactions leading to the formation of the epoxide and the addition of molecular oxygen, aiming to evaluate the likely preferred path.

The reaction scheme is depicted in Fig. 9, and the corresponding results are summarized in Fig. 10.

In Fig. 10, the potential energy surface is depicted for the formation of 1,2-LO endo (left) and the addition of molecular oxygen resulting in the formation of the radical species ROO for both Z and E configurations.

Regarding the formation of the epoxide, the optimized geometry of the transition state (TS 1,2-LO endo) reveals specific structural changes. The O-NO_2 bond distance increases from 1.41 to 1.78 Å, while the C_1-O bond distance decreases from 2.48 to 2.00 Å. Furthermore, there is a significant reduction in the C_1-C_2-O bond angle from 113.3° to 87.4°, signifying the concerted closure of the epoxy ring. The steady state 1,2-LO endo, located at –22.99 kcal/mol relatively to the radical intermediate INT-C_2 endo, necessitates overcoming an activation barrier of 16.49 kcal/mol. Despite the epoxidation process being entropically favoured and aided by the evolution of gaseous NO_2 from the reaction mixture, the calculated activation barrier implies that the closure of the epoxy ring, even if possible, is not facile at room temperature. This implies that the mechanism is probably assisted by interactions with the catalyst surface, which are not considered in the computational

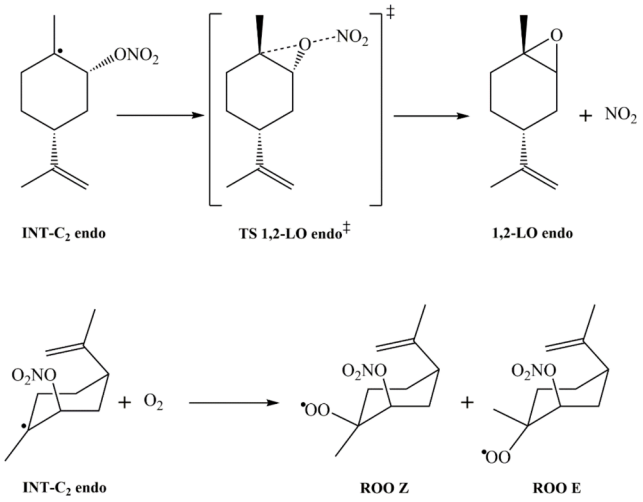

Fig. 9. Schematic representation of the formation of the epoxide ring (top) and the addition of molecular oxygen (bottom) starting from the thermodynamically more favoured INT-C_2 endo adduct.

approach. These interactions may promote the closure of the epoxy ring, especially considering that the radical nitrates are presumed to exist only in the proximity of the catalyst.

We investigated the addition of molecular oxygen to the INT-C_2 endo intermediate, resulting in the formation of the peroxyalkyl radical, considering both E and Z isomerism. The optimized geometries of the transition states (TS-ROO $E^{‡}$ and TS-ROO $Z^{‡}$) reveal specific structural changes upon the approach of molecular oxygen. It is worth underlying that the latter has been considered in triplet state ($^3O_2$). An elongation of the O-O bond (1.21 Å) by 0.05 and 0.08 Å is observed for the E and Z isomers, respectively, indicating a weakening of the O-O bond due to the interaction with C_1. Additionally, a variation in the dihedral angle C_7-C_1-C_2-O occurs, with a positive change (from −39.4° to 1.0°) for the E isomer and a negative change (from −39.4° to −43.1°) for the Z isomer. The calculated energies for the ROO E and ROO Z intermediates are −30.50 and −31.33 kcal/mol, respectively. These values are approximately 7–8 kcal/mol more negative than 1,2-LO endo, indicating that the addition of molecular oxygen is thermodynamically more stable than the closure of the epoxy ring. Furthermore, the transition states identified have energies are at 10.20 and −3.89 kcal/mol, for E and Z configurations, respectively, which implies ROO geometries are also kinetically more favoured than the transition state leading to the formation of the epoxide.

Results indicate a clear preference for the addition of molecular oxygen in the Z geometry. It is noteworthy that this preference is observed despite the negative entropic contribution resulting from a global reduction in spin multiplicity and in liberty degrees during the process. However, it is important to note that these calculations consider reactions without accounting for possible surface interactions with the catalyst, diffusion mechanisms, the concentration of molecular oxygen dissolved in the solvent medium, concentration gradients, and competitive phenomena. Nonetheless, the concentration of molecular oxygen in the reaction mixture seems to play a crucial role, particularly the fraction available for addition to the carbon-centred radical, as it determines the direction of the reaction and the selectivity of the process. The outcomes of the computational investigation underscore the thermodynamic and kinetic favourability of nitrate radical addition to the endocyclic double bond, regardless of the endo or exo geometries. Furthermore, it is revealed that the most stable radical intermediate arises from an addition to the least substituted carbon in the endo isomer configuration. The resulting intermediates possess the potential to undergo rearrangements leading to epoxide formation or to be subjected to the addition of molecular oxygen to the radical carbon.

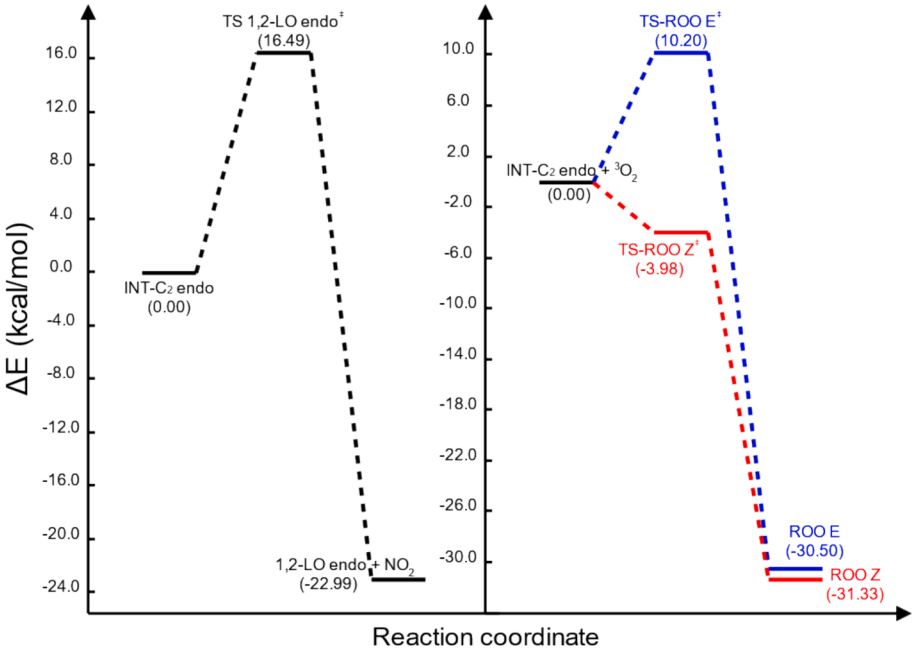

Fig. 10. PES at the CCSD(T)/CBS level with ZPE correction at the UB3LYP/6-31+G(d,p) level of epoxide formation (left) and molecular oxygen addition (right).

Comparatively, the latter process of oxygen addition exhibits both thermodynamic and kinetic preference over the closure of the epoxy ring. This preference is in line with experimental data, which demonstrates substantial epoxide formation only when external factors, such as limited molecular oxygen availability, hinder the oxidative cleavage process. Nevertheless, interactions with the catalyst surface, a consideration not encompassed within the computational approach, may influence process selectivity.

4. Conclusions

The results of this study provide valuable insights into the intricate mechanisms underlying the selective photocatalytic conversion of *R*-limonene to *R*-limononaldehyde. Specifically, the role of silver ions, nitrate radicals, and molecular oxygen in this process has been elucidated. Silver has been identified as a key participant, serving both as electron scavenger in its ionic form and as electron sink once in the form of metallic silver nanoparticles on the TiO_2 surface. Possible thermal of plasmonic catalytic effects of the silver nanoparticles could be excluded. Instead, when suppressing the scavenging role of silver ions (*i.e.* in the presence of pre-deposited silver nanoparticles onto the catalyst), a significant decrease in the reaction rate was noticed, along with a significant change in the products distribution and selectivity. In fact, selectivity towards *R*-limononaldehyde reduced from 60 % to 16 %, while relevant formation of 1,2-limonene epoxide, formed only in traces in the presence of silver ions, was observed with selectivity values up to ca. 27 %. Therefore, *R*-limononaldehyde production is promoted only in the presence of silver ions as preferential (and sacrificial) electron scavengers, thus making molecular oxygen more available for oxidative cleavage of limonene. On the other hand, when silver is pre-deposited, oxygen acts as preferential electron scavenger, addressing the reaction towards the epoxydic product. These experimental results indicate that the epoxidation reaction is kinetically limited with respect to the oxidative cleavage and that the selectivity of reaction can be addressed by tailoring kinetically limiting factors such as the oxygen concentration. This was verified experimentally, by increasing the oxygen concentration in the reacting mixture, and computationally. In particular, calculations revealed that the addition of nitrate radicals to *R*-limonene is favoured for all the possible geometries. The resulting intermediates can subsequently undergo addition of molecular oxygen, finally producing the carbonyl compound, or cyclization to the epoxide with NO_2 evolution. In agreement with the experimental results, the latter path results kinetically less favoured compared to the addition of molecular oxygen. Consequently, under lower oxygen concentration, the epoxy ring closure may become the preferred pathway. In summary, these findings provide comprehensive insights into the underlying reaction mechanisms and the factors influencing the selectivity of the photocatalytic conversion of limonene induced by nitrate radicals. The interplay between silver ions, nitrate radicals, and molecular oxygen is highlighted, contributing to a future rational design and optimization of photocatalytic systems for the selective synthesis of valuable products from renewable olefin feedstocks.

CRediT authorship contribution statement

Alessandro Gottuso: Writing – original draft, Methodology, Investigation, Formal analysis, Data curation, Conceptualization, Validation, Visualization. **Filippo Parisi:** Writing – review & editing, Investigation, Data curation. **Davide Lenaz:** Resources, Data curation. **Francesco Parrino:** Conceptualization, Methodology, Supervision, Visualization, Writing – review & editing.

Declaration of competing interest

The authors declare that they have no known competing financial interests or personal relationships that could have appeared to influence the work reported in this paper.

Data availability

Data will be made available on request.

Appendix A. Supplementary data

Supplementary data to this article can be found online at https://doi.org/10.1016/j.jphotochem.2024.115871.

References

[1] S.S. Brown, J. Stutz, Nighttime radical observations and chemistry, Chem. Soc. Rev. 41 (19) (2012) 6405–6447, https://doi.org/10.1039/C2CS35181A.

[2] A. Geyer, R. Ackermann, R. Dubois, B. Lohrmann, T. Müller, U. Platt, Long-term observation of nitrate radicals in the continental boundary layer near Berlin, Atmos. Environ. 35 (21) (2001) 3619–3631, https://doi.org/10.1016/S1352-2310(00)00549-5.

[3] M. Dam, D.C. Draper, A. Marsavin, J.L. Fry, J.N. Smith, Observations of gas-phase products from the nitrate-radical-initiated oxidation of four monoterpenes, Atmos. Chem. Phys. 22 (13) (2022) 9017–9031, https://doi.org/10.5194/acp-22-9017-2022.

[4] M.A.H. Khan, M.C. Cooke, S.R. Utembe, A.T. Archibald, R.G. Derwent, P. Xiao, C. J. Percival, M.E. Jenkin, W.C. Morris, D.E. Shallcross, Global modeling of the nitrate radical (NO_3) for present and pre-industrial scenarios, Atmos. Res. 164–165 (2015) 347–357, https://doi.org/10.1016/j.atmosres.2015.06.006.

[5] R.P. Wayne, I. Barnes, P. Biggs, J.P. Burrows, C.E. Canosa-Mas, J. Hjorth, G. Le Bras, G.K. Moortgat, D. Perner, G. Poulet, G. Restelli, H. Sidebottom, The nitrate radical: Physics, chemistry, and the atmosphere, Atmos. Environ. a. Gen. Top. 25 (1) (1991) 1–203, https://doi.org/10.1016/0960-1686(91)90192-A.

[6] K.H. Bates, G.J.P. Burke, J.D. Cope, T.B. Nguyen, The nitrate radical (NO_3) oxidation of alpha-pinene is a significant source of secondary organic aerosol and organic nitrogen under simulated ambient nighttime conditions, Atmospheric Chem. Phys. Discussions (2021) 1–24, https://doi.org/10.5194/acp-2021-703.

[7] N.L. Ng, S.S. Brown, A.T. Archibald, E. Atlas, R.C. Cohen, J.N. Crowley, D.A. Day, N.M. Donahue, J.L. Fry, H. Fuchs, R.J. Griffin, M.I. Guzman, H. Herrmann, A. Hodzic, Y. Iinuma, J.L. Jimenez, A. Kiendler-Scharr, B.H. Lee, D.J. Luecken, J. Mao, R. McLaren, A. Mutzel, H.D. Osthoff, B. Ouyang, B. Picquet-Varrault, U. Platt, H.O.T. Pye, Y. Rudich, R.H. Schwantes, M. Shiraiwa, J. Stutz, J. A. Thornton, A. Tilgner, B.J. Williams, R.A. Zaveri, Nitrate radicals and biogenic volatile organic compounds: oxidation, mechanisms and organic aerosol, Atmospheric Chem. Phys. Discussions (2016) 1–111, https://doi.org/10.5194/acp-2016-734.

[8] S.P. Mezyk, T.D. Cullen, K.A. Rickman, B.J. Mincher, The reactivity of the nitrate radical ($^{\bullet}NO_3$) in acqueous and organic solutions, Int. J. Chem. Kinet. 49 (9) (2017) 635–642, https://doi.org/10.1002/kin.21103.

[9] E. Baciocchi, T.D. Giacco, S.M. Murgia, S.V. Sebastiani, Rate and mechanism for the reaction of the nitrate radical with aromatic and alkylaromatic compounds in acetonitrile, J. Chem. Soc. Chem. Commun. 16 (1987) 1246–1248, https://doi.org/10.1039/C39870001246.

[10] D. Rousse, C. George, A novel long path photolysis cell—application to the reactivity of selected organic compounds toward the nitrate radical (NO_3), Phys. Chem. Chem. Phys. 6 (13) (2004) 3408–3414, https://doi.org/10.1039/B400175C.

[11] M. P. Pérez-Casany, I. Nebot-Gil, J. Sánchez-Marín, F. Tomás-Vert, E. Martínez-Ataz, B. Cabanas-Galán and A. Aranda-Rubio, Ab initio study on the mechanism of tropospheric reactions of the nitrate radical with alkenes: Ethene, J. Org. Chem., 63 (20), 1998, 63, 6978–6983. 10.1021/jo980779j.

[12] H. Gong, A. Matsunaga, P.J. Ziemann, Products and mechanism of secondary organic aerosol formation from reactions of linear alkenes with NO_3 radicals, J. Phys. Chem. A 109 (19) (2005) 4312–4324, https://doi.org/10.1021/jp058024l.

[13] U. Wille, T. Dreessen, Mechanistic insights into $NO_3^{\bullet}$ induced self-serminating radical oxygenations, Part 1: A computational study on $NO_3^{\bullet}$ and its addition to alkynes, J. Phys. Chem. A 110 (6) (2006) 2195–2203, https://doi.org/10.1021/jp0454772.

[14] C. Weller, H. Herrmann, Kinetics of nitrosamine and amine reactions with NO_3 radical and ozone related to aqueous particle and cloud droplet chemistry, Atmos. Res. 151 (2015) 64–71, https://doi.org/10.1016/j.atmosres.2014.02.023.

[15] S. Langer, E. Ljungstrom, I. Wangberg, Rates of reaction between the nitrate radical and some aliphatic esters, J. Chem. Soc. Faraday Trans. 89 (3) (1993) 425–431, https://doi.org/10.1039/FT9938900425.

[16] D. Friedmann, A. Hakki, H. Kim, W. Choi, D. Bahnemann, Heterogeneous photocatalytic organic synthesis: State-of-the-art and future perspectives, Green Chem. 18 (20) (2016) 5391–5411, https://doi.org/10.1039/C6GC01582D.

[17] F. Parrino, L. Palmisano, Reactions in the presence of irradiated semiconductors: Are they simply photocatalytic? Mini-Rev. Org. Chem. 15 (2) (2018) 157–164, https://doi.org/10.2174/1570193X14666171117151718.

[18] M.R. Hoffmann, S.T. Martin, W. Choi, D.W. Bahnemann, Environmental applications of semiconductor photocatalysis, Chem. Rev. 95 (1) (1995) 69–96, https://doi.org/10.1021/cr00033a004.

[19] W.S. Jenks, Photocatalytic reaction pathways – Effects of molecular structure, catalyst, and wavelength, Photocatalysis and Water Purification (2013) 25–51, https://doi.org/10.1002/9783527645404.ch2.

[20] A. Hakki, J. Schneider, D. Bahnemann, Understanding the chemistry of photocatalytic processes, Fundamentals and Perspectives, The Royal Society of Chemistry, Photocatalysis, 2016, pp. 29–50.

[21] F. Parrino, S. Livraghi, E. Giamello, L. Palmisano, The existence of nitrate radicals in irradiated TiO_2 aqueous suspensions in the presence of nitrate ions, Angew. Chem. Int. Ed. 57 (33) (2018) 10702–10706, https://doi.org/10.1002/anie.201804879.

[22] F. Parrino, S. Livraghi, E. Giamello, R. Ceccato, L. Palmisano, The role of hydroxyl, superoxide, and nitrate radicals on the fate of bromide ions in photocatalytic TiO_2 suspensions, ACS Catal. 10 (14) (2020) 7922–7931, https://doi.org/10.1021/acscatal.0c02010.

[23] J.L. DiMeglio, A.G. Breuhaus-Alvarez, S. Li, B.M. Bartlett, Nitrate-mediated alcohol oxidation on cadmium sulfide photocatalysts, ACS Catal. 9 (6) (2019) 5732–5741, https://doi.org/10.1021/acscatal.9b01051.

[24] B.D. Terry, J.L. DiMeglio, J.P. Cousineau, B.M. Bartlett, Nitrate radical facilitates indirect benzyl alcohol oxidation on bismuth(III) vanadate photoelectrodes, ChemElectroChem 7 (18) (2020) 3776–3782, https://doi.org/10.1002/celc.202000911.

[25] A. Gottuso, C. De Pasquale, S. Livraghi, L. Palmisano, S. Diré, R. Ceccato, F. Parrino, Nitrate radicals generated by TiO_2 heterogeneous photocatalysis: Application to the cleavage of C=C double bond to carbonyl compounds, Mol. Catal. 550 (2023) 113607, https://doi.org/10.1016/j.mcat.2023.113607.

[26] N. Morante, A. Gottuso, F. Parrino, V. Vaiano, Nitrate radical formation and reaction with limonene by TiO_2 photocatalysis: a kinetic study, Catal. Today 432 (2024) 114600, https://doi.org/10.1016/j.cattod.2024.114600.

[27] A. Gottuso, F. Parrino, Toward a sustainable photocatalytic oxidative cleavage of olefins mediated by nitrate radicals: the influence of the physicochemical features of the photocatalyst, J. Phys. Chem. C 128 (11) (2024) 4497–4507, https://doi.org/10.1021/acs.jpcc.3c07543.

[28] A. D. Becke, Density-functional thermochemistry. III. The role of exact exchange, J. Chem. Phys., 98(7), (1993), 5648-5652. 10.1063/1.464913.

[29] C. Lee, W. Yang, R.G. Parr, Development of the Colle-Salvetti correlation-energy formula into a functional of the electron density, Phys. Rev. B 37 (2) (1988) 785–789, https://doi.org/10.1103/physrevB.37.785.

[30] Chr. Møller, M. S. Plesset, Note on an approximation treatment for many-electron systems, Phys. Rev., 46(7), (1934), 618-622. 10.1103/PhysRev.46.618.

[31] J.A. Pople, M. Head-Gordon, K. Raghavachari, Quadratic configuration interaction. A general technique for determining electron correlation energies, J. Chem. Phys. 87 (10) (1987) 5968–5975, https://doi.org/10.1063/1.453520.

[32] T.H. Dunning, Gaussian basis sets for use in correlated molecular calculations. I. The atoms boron through neon and hydrogen, J. Chem. Phys. 90 (2) (1989) 1007–1023, https://doi.org/10.1063/1.456153.

[33] J.M.L. Martin, Ab initio total atomization energies of small molecules – towards the basis set limit, Chem. Phys. Lett. 259 (5–6) (1996) 669–678, https://doi.org/10.1016/0009-2614(96)00898-6.

[34] C. Cavallotti, D. Polino, A. Frassoldati, E. Ranzi, Analysis of some reaction pathways active during cyclopentadiene pyrolysis, J. Phys. Chem. A 116 (13) (2012) 3313–3324, https://doi.org/10.1021/jp212151p.

[35] A.V. Marenich, C.J. Cramer, D.G. Truhlar, Universal Solvation Model Based on Solute Electron Density and on a Continuum Model of the Solvent Defined by the Bulk Dielectric Constant and Atomic Surface Tensions, J. Phys. Chem. b. 113 (18) (2009) 6378–6396, https://doi.org/10.1021/jp810292n.

[36] L. Jiang, W. Wang, Y. Xu, Theoretical investigation of the NO_3 radical addition to double bonds of limonene, Int. J. Mol. Sci. 10 (9) (2009) 3743–3754, https://doi.org/10.3390/ijms10093743.

[37] L. Jiang, W. Wang, Y. Xu, Ab initio investigation of O_3 addition to double bonds of limonene, Chem. Phys. 368 (3) (2010) 108–112, https://doi.org/10.1016/j.chemphys.2010.01.003.

[38] Gaussian 16, Revision A.03, M. J. Frisch, G. W. Trucks, H. B. Schlegel, G. E. Scuseria, M. A. Robb, J. R. Cheeseman, G. Scalmani, V. Barone, G. A. Petersson, H. Nakatsuji, X. Li, M. Caricato, A. V. Marenich, J. Bloino, B. G. Janesko, R. Gomperts, B. Mennucci, H. P. Hratchian, J. V. Ortiz, A. F. Izmaylov, J. L. Sonnenberg, D. Williams-Young, F. Ding, F. Lipparini, F. Egidi, J. Goings, B. Peng, A. Petrone, T. Henderson, D. Ranasinghe, V. G. Zakrzewski, J. Gao, N. Rega, G. Zheng, W. Liang, M. Hada, M. Ehara, K. Toyota, R. Fukuda, J. Hasegawa, M. Ishida, T. Nakajima, Y. Honda, O. Kitao, H. Nakai, T. Vreven, K. Throssell, J. A. Montgomery, Jr., J. E. Peralta, F. Ogliaro, M. J. Bearpark, J. J. Heyd, E. N. Brothers, K. N. Kudin, V. N. Staroverov, T. A. Keith, R. Kobayashi, J. Normand, K. Raghavachari, A. P. Rendell, J. C. Burant, S. S. Iyengar, J. Tomasi, M. Cossi, J. M. Millam, M. Klene, C. Adamo, R. Cammi, J. W. Ochterski, R. L. Martin, K. Morokuma, O. Farkas, J. B. Foresman, and D. J. Fox, Gaussian, Inc., Wallingford CT, 2016.

[39] V. Augugliaro, M. Bellardita, V. Loddo, G. Palmisano, L. Palmisano, S. Yurdakal, Overview on oxidation mechanisms of organic compounds by TiO_2 in heterogeneous photocatalysis, J. Photochem. Photobiol. C 13 (3) (2012) 224–245, https://doi.org/10.1016/j.jphotochemrev.2012.04.003.

[40] R. Molinari, P. Argurio, C. Lavorato, Review on reduction and partial oxidation of organics in photocatalytic (membrane) reactors, Curr. Org. Chem. 17 (21) (2013) 2516–2537, https://doi.org/10.2174/13852728113179990063.

[41] N. Feng, H. Lin, H. Song, L. Yang, D. Tang, F. Deng, J. Ye, Efficient and selective photocatalytic CH_4 conversion to CH_3OH with O_2 by controlling overoxidation on TiO_2, Nat. Commun. 12 (2021) 4652, https://doi.org/10.1038/s41467-021-24912-0.

[42] Y. Chen, Y. Wang, W. Li, Q. Yang, Q. Hou, L. Wei, L. Liu, F. Huang, M. Ju, Enhancement of photocatalytic performance with the use of noble-metal-decorated TiO_2 nanocrystals as highly active catalysts for aerobic oxidation under visible-light irradiation, Appl. Catal. B 210 (2017) 352–367, https://doi.org/10.1016/j.apcatb.2017.03.077.

[43] L.S. Ardakani, A. Surendar, L. Thangavelu, T. Mandal, Silver nanoparticles (Ag NPs) as catalyst in chemical reactions, Synth. Commun. 51 (10) (2021) 1516–1536, https://doi.org/10.1080/00397911.2021.1894450.

[44] E. Kowalska, O.O.P. Mahaney, R. Abe, B. Ohtani, Visible-light-induced photocatalysis through surface plasmon excitation of gold on titania surfaces, Phys. Chem. Chem. Phys. 12 (10) (2010) 2344–2355, https://doi.org/10.1039/B917399D.

[45] A. Tanaka, K. Hashimoto, B. Ohtani, H. Kominami, Non-linear photocatalytic reaction induced by visible-light surface-plasmon resonance absorption of gold

nanoparticles loaded on titania particles, ChemComm. 49 (33) (2013) 3419–3421, https://doi.org/10.1039/C3CC41122B.
[46] K.L. Kelly, E. Coronado, L.L. Zhao, G.C. Schatz, The optical properties of metal nanoparticles: The influence of size, shape, and dielectric environment, J. Phys. Chem. B 107 (3) (2003) 668–677, https://doi.org/10.1021/jp026731y.
[47] A. Jakimińska, K. Spilarewicz, W. Macyk, Phototransformations of TiO_2/Ag_2O composites and their influence on photocatalytic water splitting accompanied by methanol photoreforming, Nanoscale Adv. 5 (7) (2023) 1926–1935, https://doi.org/10.1039/D2NA00910B.
[48] S. Mihai, D.L. Cursaru, D. Ghita, A. Dinescu, Morpho ierarhic TiO_2 with plasmonic gold decoration for highly active photocatalysis properties, Mater. Lett. 162 (2016) 222–225, https://doi.org/10.1016/j.matlet.2015.10.012.
[49] K.K. Paul, P.K. Giri, H. Sugimoto, M. Fujii, B. Choudhury, Evidence for plasmonic hot electron injection induced superior visible light photocatalysis by g-C_3N_4 nanosheets decorated with Ag-TiO_2(B) and Au-TiO_2(B) nanorods, Sol. Energy Mater. Sol. 201 (2019) 110053, https://doi.org/10.1016/j.solmat.2019.110053.
[50] G. Milazzo, S. Caroli, V.K. Sharma, Tables of Standard Electrode Potentials, Wiley, London, 1978.
[51] A.J. Bard, B. Parsons, J. Jordon, Standard Potentials in Aqueous Solutions, M, Dekker, New York, 1985.
[52] M. Prein, W. Adam, The Schenck ene reaction: Diastereoselective oxyfunctionalization with singlet oxygen in synthetic applications, Angew. Chem. Int. Ed. 35 (5) (1996) 477–494, https://doi.org/10.1002/anie.199604771.
[53] E.L. Clennan, A. Pace, Advances in singlet oxygen chemistry, Tetrahedron 61 (28) (2005) 6665–6691, https://doi.org/10.1016/j.tet.2005.04.017.
[54] A.A. Frimer, The reaction of singlet oxygen with olefins: the question of mechanism, Chem. Rev. 79 (5) (1979) 359–387, https://doi.org/10.1021/cr60321a001.
[55] Y. Wu, G. Zhou, Q. Meng, X. Tang, G. Liu, H. Yin, J. Zhao, F. Yang, Z. Yu, Y. Luo, Visible light-induced aerobic epoxidation of α, β-unsaturated ketones mediated by amidines, J. Org. Chem. 83 (21) (2018) 13051–13062, https://doi.org/10.1021/acs.joc.8b01710.
[56] R. Ciriminna, F. Parrino, C. De Pasquale, L. Palmisano, M. Pagliaro, Photocatalytic partial oxidation of limonene to 1,2 limonene oxide, ChemmComm. 54 (8) (2018) 1008–1011, https://doi.org/10.1039/C7CC09788C.
[57] A. Gottuso, A. Köckritz, M.L. Saladino, F. Armetta, C. De Pasquale, G. Nasillo, F. Parrino, Catalytic and photocatalytic epoxidation of limonene: Using mesoporous silica nanoparticles as functional support for a Janus-like approach, J. Catal. 391 (2020) 202–211, https://doi.org/10.1016/j.jcat.2020.08.025.
[58] F. Parrino, M. D'Arienzo, S. Mostoni, S. Dirè, R. Ceccato, M. Bellardita, L. Palmisano, Electron and energy transfer mechanisms: The double nature of TiO_2 heterogeneous photocatalysis, Top. Curr. Chem. 380 (1) (2022) 1–15, https://doi.org/10.1007/s41061-021-00358-2.
[59] X. Hu, H. Ji, L. Wu, Singlet oxygen photogenerated and 2,4,6-TCP photodegradation at Pt/TiO_2 under visible light illumination, RSC Adv. 2 (32) (2012) 12378–12383, https://doi.org/10.1039/C2RA21661B.
[60] M. Spittler, I. Barnes, I. Bejan, K.J. Brockmann, Th. Benter, K. Wirtz, Reactions of NO_3 radicals with limonene and α-pinene: Product and SOA formation, Atmos. Environ. 40 (1) (2006) 116–127, https://doi.org/10.1016/j.atmosenv.2005.09.093.
[61] I. Mayer, The spin-projected extended Hartree-Fock method, Adv. Quantum Chem. 12 (1980) 189–262, https://doi.org/10.1016/S0065-3276(08)60317-2.
[62] F. Jensen, A remarkable large effect of spin contamination on calculated vibrational frequencies, Chem. Phys. Lett. 169 (6) (1990) 519–528, https://doi.org/10.1016/0009-2614(90)85641-O.
[63] M.R. Hand, C.F. Rodriquez, I.H. Williams, G.G. Balint-Kurti, Theoretical estimation of the activation energy for the reaction HO + H_2O → H2O + OH: Importance of tunnelling, J. Phys. Chem. A 102 (29) (1998) 5958–5966, https://doi.org/10.1021/jp980838x.
[64] M.L. Dubernet, D. Flower, J.M. Hutson, The Dynamics of Open-Shell van der Waals Complexes, J. Chem. Phys. 94 (12) (1991) 7602–7618, https://doi.org/10.1063/1.460147.
[65] J.R. Alvarez-Idaboy, N. Mora-Diez, A. Vivier-Bunge, A quantum chemical and classical transition state theory explanation of negative activation energies in OH addition to substituted ethenes, J. Am. Chem. Soc. 122 (15) (2000) 3715–3720, https://doi.org/10.1021/ja993693w.
[66] I.R. Piletic, R. Howell, L.J. Bartolotti, T.E. Kleindienst, S.M. Kaushik, E.O. Edney, Multigenerational Theoretical Study of Isoprene Peroxy Radical 1–5-Hydrogen Shift Reactions that Regenerate HOx Radicals and Produce Highly Oxidized Molecules, J. Phys. Chem. A 123 (4) (2019) 906–919, https://doi.org/10.1021/acs.jpca.8b09738.
[67] M.A. Allodi, K.N. Kirschner, G.C. Shields, Thermodynamics of the Hydroxyl Radical Addition to Isoprene, J. Phys. Chem. A 112 (30) (2008) 7064–7071, https://doi.org/10.1021/jp801869c.
[68] I.R. Piletic, E.O. Edney, L.J. Bartolotti, Barrierless Reactions with Loose Transition States Govern the Yields and Lifetimes of Organic Nitrates Derived from Isoprene, J. Phys. Chem. A 121 (43) (2017) 8306–8321, https://doi.org/10.1021/acs.jpca.7b08229.